Available online at www.sciencedirect.com

jmr&t Journal of Materials Research and Technology

journal homepage: www.elsevier.com/locate/jmrt

Original Article

Ultrastrong and ductile synergy of additively manufactured H13 steel by tuning cellular structure and nano-carbides through tempering treatment

Tao Wen [a], *Feipeng Yang* [a], *Jianying Wang* [a], *Hailin Yang* [a,*], *Junwei Fu* [b,**], *Shouxun Ji* [c]

[a] *State Key Laboratory of Powder Metallurgy, Central South University, Changsha 410083, China*

[b] *Key Laboratory of Marine Environmental Corrosion and Bio-fouling, Institute of Oceanology, Chinese Academy of Sciences, Qingdao 266071, China*

[c] *Brunel Centre for Advanced Solidification Technology (BCAST), Brunel University London, Uxbridge, Middlesex, UB8 3PH, UK*

ARTICLE INFO

Article history:
Received 29 July 2022
Accepted 10 November 2022
Available online 19 November 2022

Keywords:
H13 steel
Selective laser melting
Tempering
Microstructures
Mechanical properties

ABSTRACT

Microstructural evolution and mechanical properties of H13 steel fabricated by selective laser melting (SLM) with subsequent tempering treatment were systematically examined. It was found that the microstructure of the as-SLMed H13 samples consisted of cellular structures, lath martensite and high-volume fraction of retained austenite. After tempering at 600 °C for 1 h, the nanoscale $Cr_{23}C_6$ particles were detected at the boundaries of the partially dissolved cellular structures. The fine grains, the retained cellular structures, and the formation of $Cr_{23}C_6$ carbides significantly improved the mechanical properties of the H13 steel. A superior mechanical properties, including the yield strength (YS) of 1647 ± 29 MPa, ultimate tensile strength (UTS) of 2013 ± 35 MPa and elongation (El) of 4.1 ± 0.3% have been achieved in the SLMed H13 steel after tempering at 600 °C for 1 h. With the increase of tempering temperature to 700 °C, the cellular structures were completely dissolved and the high number density of coarse $Cr_{23}C_6$ carbides were formed, which led to the decrease of UTS at 1083 ± 21 MPa, while the elongation was significantly improved to 12.3 ± 1.2% due to the recovery of dislocation density and the decomposition of martensite in the H13 steel.

1. Introduction

H13 tool steel has been used for making moulds/dies in industry because of its high strength, excellent wear resistance and machinability [1–3]. Conventionally, H13 steel is fabricated by casting and forging before machining, which have limited design freedom and lowered production efficiency. In particular, the capability of creating conformal cooling channels and breathing capacity in the moulds are two key challenges in conventional manufacturing processes

* Corresponding author.
** Corresponding author.
E-mail addresses: y-hailin@csu.edu.cn (H. Yang), fujw@qdio.ac.cn (J. Fu).

https://doi.org/10.1016/j.jmrt.2022.11.105

[4,5]. Therefore, complex geometry and distribution of cooling channels are difficult to be made in current production. Selective laser melting (SLM) is one of additive manufacturing (AM) processes that have attracted significant attention in recent years due to enabling the customized metallic parts with complex geometries [6–8]. It is considered as a promising technique to produce H13 moulds/dies with diversified and complex geometries for both die cavity and cooling channels [9].

Currently, H13 steel with high relative density (over 99%) fabricated by SLM has been successfully achieved by optimizing the processing parameters (e.g. laser power, scan speed, hatch spacing and powder federate) [10–16]. The as-SLMed H13 is usually featured by fine primary grains, cellular structures and carbides [10,17]. However, the resulting mechanical properties are normally unsatisfactory due to the high-volume fraction of retained austenite (15–20%) [15,18] and residual stresses (~1420 MPa) [12,19,20]. Moreover, the ductility is inferior to that obtained by conventional manufacturing techniques [21–23]. For instance, Holzweissig et al. [24] reported that the as-SLMed H13 delivered the ultimate tensile strength (UTS) of 1600 MPa and the elongation (E1) of 2% along the horizontal direction, and the UTS of 1200 MPa and El of 1.4% along the building direction. Similar results were reported by Yan et al. [12]. Furthermore, the expansion occurs inevitably due to the transformation from the retained austenite to martensite, resulting in the distortion and cracking in as-SLMed steel [16,20].

Tempering is an effective method to eliminate the retained austenite and produce pronounced secondary hardening by introducing carbides (e.g. $M_{23}C_6$, M_7C_3, MC) in H13 steel [10,25,26]. It was confirmed that tempering at 500–600 °C with appropriate holding time could simultaneously improve the hardness and softening the resistance of as-SLMed H13 steel [25]. Katancik et al. [27] reported that the excellent microhardness of 728.5 ± 28.2 Hv were obtained in as-SLMed H13 steel after tempering at 550 °C for 2 h. Fine martensitic structure, high dislocation density and the carbides formed during tempering could potentially hinder dislocation movement and lead to high hardness. Yan et al. [28] found that as-SLMed H13 steel tempered at 600 °C for 2 h could achieve the yield strength of 1483 ± 48 MPa, UTS of 1938 ± 62 MPa and elongation of 5.8 ± 0.61%. The precipitation of fine V_8C_7 and the high number density of dislocations were the main contributors for high strength in as-SLMed H13 steel. In addition, the cellular structures produced by SLM were also significant in improving the strength of H13 steel under as-SLMed condition. Our previous work [16] has demonstrated that the high density dislocations and the cellular structure enriched in Cr and Mo elements are responsible for the enhanced mechanical properties of as-SLMed H13. Similarly, the cellular structure was found to significantly enhance the strength of as-SLMed 316L steel [29,30]. However, tempering with prolonged holding time can destroy the unique cellular structure and soften the as-SLMed H13 steel. Although the carbides introduced by tempering at high temperatures can increase the strength of as-SLMed H13 steel, the complete dissolution of cellular structures inevitably causes a dramatic reduction in the strength of as-SLMed H13 steel. Therefore, it is essential to find an appropriate tempering process to obtain the optimum combination of mechanical properties of as-SLMed H13 steel due to the trade-off between the decrease of strength induced by dissolved cellular structures and the improvement in strength induced by carbide precipitates. However, the strengthening mechanism needs to be further examined and elaborated.

In this study, H13 steel was fabricated by SLM and subsequently tempered at 600 and 700 °C. It is aimed to study the microstructural evolution and mechanical properties of the as-SLMed H13 steel during tempering. Moreover, a model for microstructural evolution was established to understand the insight of strengthening mechanisms. The relationship between the dissolved cellular structures and carbide precipitates was analyzed, and the strengthening mechanisms were systematically discussed.

2. Experimental materials and methods

Gas atomized H13 powders were provided by Hunan Hualiu New Materials Co., Ltd. The particle size distribution was measured as 15–53 μm. The powder morphology and particle size distribution are shown in Fig. 1. The chemical compositions of H13 powders were measured using inductively coupled plasma atomic emission spectrometry (ICAP 7000 Series, Waltham, USA) and the results are shown in Table 1. The SLM process with a FS271 M system was applied to fabricate H13 samples for microstructural characterization

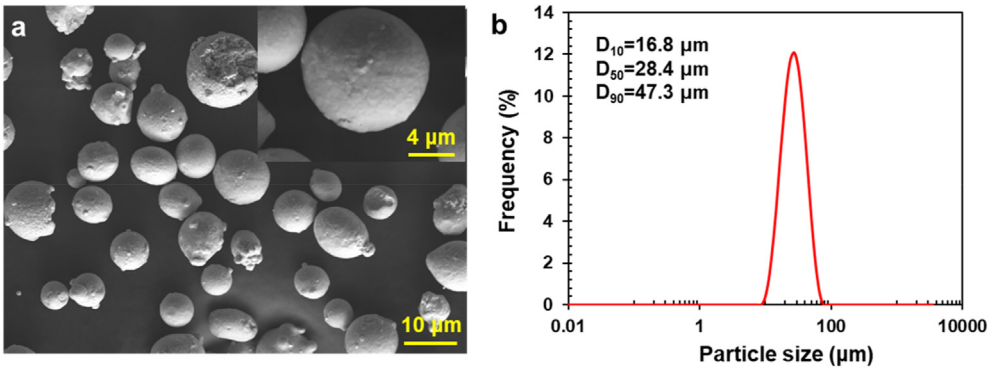

Fig. 1 – (a) SEM micrograph showing the morphology and (b) particle size distribution of H13 powders.

Table 1 – Chemical compositions of the H13 powders measured by inductively coupled plasma atomic emission spectrometry (wt.%).

Element	Cr	Mo	V	Mn	Si	C	Fe
wt.%	5.12	1.26	1.03	0.39	0.98	0.42	Bal.

and mechanical testing. The laser scanning was rotated 67° layer-by-layer, as shown in Fig. 2a. Refer to our previous study [16], the processing parameters were set as follows: laser power of 230 W, scan speed of 800 mm/s, hatch spacing at 0.1 mm, layer thickness of 0.03 mm and substrate preheating of 373 K. The cubic samples and the dog-bone-shaped tensile samples with a gauge length of 30 mm were fabricated, as shown in Fig. 2b. Subsequently, as-SLMed H13 samples were tempered at 600 °C for 1, 2, 3, 4 h and 700 °C for 1 h, respectively. Tempering was conducted in a muffle furnace (SRJX-4-13 Yong Guangming Co., Ltd., Beijing), followed by air cooling. The tempered samples were denoted as ST-600, ST-600-2, ST-600-3, ST-600-4 and ST-700, respectively.

The phase constituent of the as-SLMed and as-tempered samples were identified using X-ray diffraction (XRD, Rigaku X-2000, SmartLab 3Kw, Japan) with Cu $K\alpha$ radiation. Microstructures were characterized using a scanning electron microscope (SEM, Quanta 250 FEG, FEI, Czech). Samples were etched with 4% nitric acid alcohol. The grain size and grain orientation were measured using an electron backscattered diffraction (EBSD, Helios NaboLab G3 UC, FEI, USA). Detailed microstructure analysis was further conducted using a transmission electron microscope (TEM, Tecnai G2 F20, FEI, USA). TEM samples were prepared by a precision ion polishing system (PIPS, Gatan 691, Gatan, USA) at a voltage of 5 kV and an incident angle of 3–8°.

The dog-bone-shaped tensile samples were cut by electrical discharge machining (EDM) from the as-SLMed and as-tempered samples. Uniaxial tensile tests were carried out using a material testing system (MTS, Alliance RT30, China) with an engineering strain rate of 1×10^{-3} s^{-1} at room temperature (RT). The tensile data were the average of three measurements.

3. Results and discussion

3.1. Microstructural characterization

Fig. 3 shows the microstructures of the as-SLMed samples without and with tempering at 600 and 700 °C. The as-SLMed microstructure consisted of cellular structures and lath martensite (Fig. 3a). The average size of cellular structures was about 600 nm. The highly localized melting and ultrahigh cooling rate resulted in the formation of typical non-equilibrium microstructures during SLM process. Many studies have shown that the cellular structures of as-SLMed H13 steel were enriched in Cr and Mo elements [16,29]. In the ST-600 sample, the matrix microstructure started to transform from the supersaturated lath martensite to the tempered lath martensite. After tempering, the cellular structures showed partial dissolution and fine carbides were formed (Fig. 3b). With the increase of tempering time, the features of cellular structures disappeared gradually with the precipitation of numerous carbide particles. In the ST-700 sample, the cellular structures were completely disappeared and coarse globular carbide particles were formed (Fig. 3f).

Fig. 4 shows the XRD patterns obtained from the as-SLMed, ST-600 and ST-700 samples. The peaks of martensite (α-Fe) and retained austenite (γ-Fe) phases were observed in the as-SLMed sample. The presence of retained austenite could be ascribed to the phase transformation under high cooling rates in SLM process, leading to the incompletion of phase transformation from austenite to martensite [21,27]. In Fig. 4c for the EBSD phase distribution image, the martensite content and retained austenite content in the as-SLMed sample were 85% and 15%, respectively. The peak intensity of the retained austenite in the ST-600 sample was reduced. Moreover, only the peak of martensite phase in the XRD patterns of the ST-700 sample could be detected. Correspondingly, the EBSD phase distribution image in Fig. 4d and e indicated that only 8% and 4% of austenite was remained after tempering at 600 and 700 °C, respectively. Fig. 4b shows the magnified image of the martensite peak (110). It can be noted that the (110) peak of ST-600 and ST-700 samples were shifted to the higher θ in

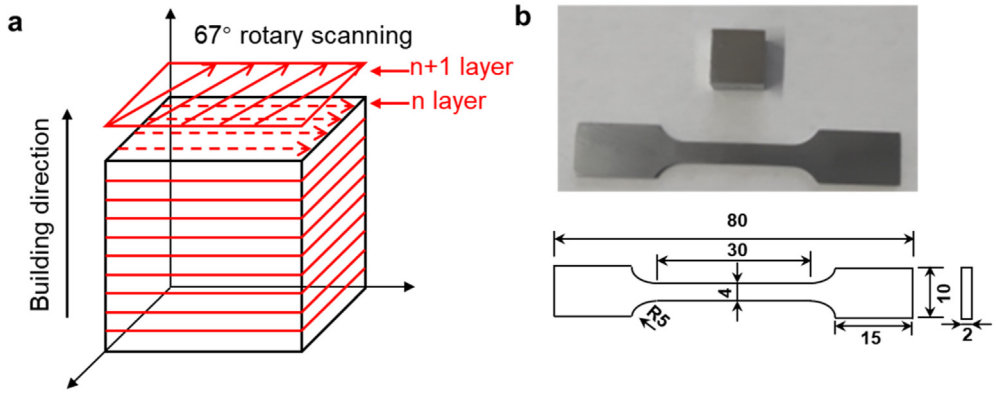

Fig. 2 – (a) Schematic of the scanning strategy during SLM process; (b) the cubic samples and the dog-bone-shaped tensile samples.

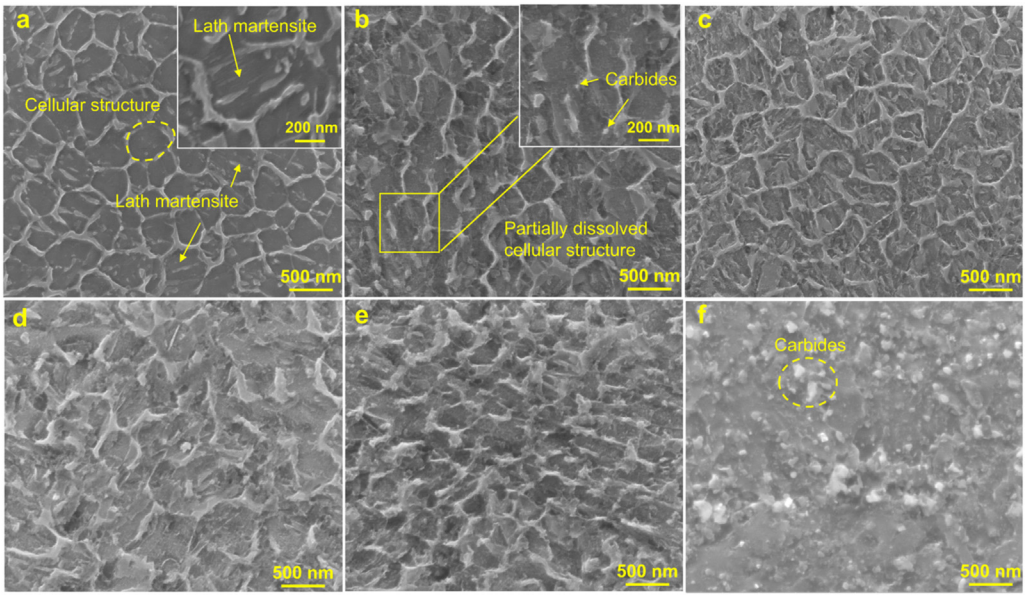

Fig. 3 – SEM images showing the microstructure of as-SLMed H13 steel with different heat treatments: (a) as-SLMed; (b) ST-600; (c) ST-600-2; (d) ST-600- 3; (e) ST-600-4; (f) ST-700.

comparison to that in the as-SLMed sample. Based on Bragg's law, the reasons for the shift of (110) peak can be explained as follows [31] :

$$2d\sin(\theta) = n\lambda \quad (1)$$

where d is the lattice spacing, 2θ is the diffraction angle, n is the diffraction order and λ is the wavelength. In the tempered samples, the diffraction peaks of martensite showed a slight shift to high angles, indicating a slight decrease in the lattice constant of martensite. Generally, a large residue stress was accumulated inside the as-SLMed alloy due to rapid solidification process with high cooling rates, which may distort the crystal lattice of the as-SLMed alloy [32,33]. The tempering decomposes the supersaturated martensite into ferrite and carbide, which may further distort the lattice [34]. Moreover, carbides tend to precipitate from the supersaturated matrix during tempering, which induces a decrease in the lattice spacing of matrix. According to Bragg's law, the decrease of

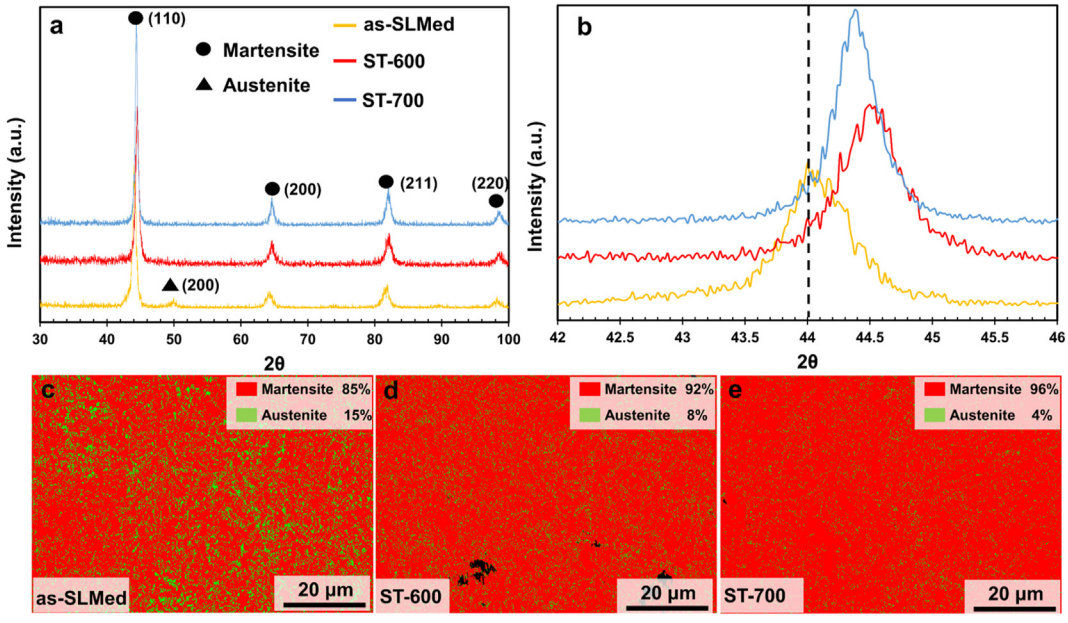

Fig. 4 – (a) XRD spectra of as-SLMed, ST-600 and ST-700 samples; (b) the magnified image of the martensite peaks (110) of (a); (c) EBSD phase distribution image of as-SLMed sample; (d) EBSD phase distribution image of ST-600 sample; (e) EBSD phase distribution image of ST-700 sample.

d leads to the increase of 2θ. Consequently, the (100) peak of ST-600 and ST-700 samples were shifted to the right.

EBSD map, grain size distribution map and Kernel average misorientation (KAM) map of as-SLMed H13 steel without and with tempering are shown in Fig. 5. As indicated in Fig. 5a, the inverse pole figure (IPF) map showed that the microstructure of the as-SLMed sample was dominated by fine grains and texture free. The average grain size was 1.84 μm. The fine grain was preserved in the ST-600 and ST-700 samples, but the grain size increased slightly to 2.75 and 2.87 μm, respectively. Based on the Hall-Patch relationship, it is evident that the fine grains can substantially improve the strength of alloys [35,36]. Additionally, the KAM maps of as-SLMed alloy without and with tempering are shown in Fig. 5c and f&5i. The average KAM value of as-SLMed alloy was 1.349. The variations in average KAM qualitatively reflected the degree of plastic deformation or defect density. Generally, tempering treatment leads to the recovery of dislocations. Therefore, the average KAM value of ST-600 and ST-700 samples was 1.335 and 0.990, respectively. According to Eq. (2), the KAM was used to calculate geometrically necessary dislocation (GND)

$$\rho_{GND} = 2\vartheta / (\mu b) \quad (2)$$

where ϑ is the KAM, μ is the step size during EBSD measurement (0.2 μm), and b is the Burger vector (0.25 nm [28]). Correspondingly, the ρ_{GND} of as-SLMed, ST-600 and ST-700 samples were estimated to be 5.39×10^{15} m^{-2}, 5.34×10^{15} m^{-2} and 3.96×10^{15} m^{-2}, respectively. The high density of GNDs would improve the strength [37,38].

To further analyse the microstructural evolution during tempering, the TEM investigations were performed. For the as-SLMed alloy, Fig. 6a&6b show the martensite lath with a width below 200 nm and the high number density of dislocations. The bright field (BF) TEM image in Fig. 6c with inserted SAED pattern indicates the existence of the retained austenite. Meanwhile, the length of cellular structures in the as-SLMed alloy is about 200–600 nm, as shown in Fig. 6d. These typical cellular structures were enriched in Cr and Mo elements [16]. The tempered lath martensite was also detected in the ST-600 sample, as shown in Fig. 7a. A closer look into the lath martensite in Fig. 7b&c revealed that high-density dislocations and lattice distortions were typical sub-structures of lath martensite. With the dissolution of cellular structures through tempering, the Cr and Mo elements originally enriched in around the cellular structure combine with C to form carbides, which preferentially distributed at grain boundaries. These carbides were pinned to the sub-grain boundaries to form a continuous chain (Fig. 7d). The BF-image and the inserted SAED pattern in Fig. 7e&f confirmed that the carbide was Cr-rich $M_{23}C_6$ carbide. In the ST-700 samples, the tempering at high temperature resulted in the completely dissolution of cellular structures. A large amount of coarse $M_{23}C_6$ carbide precipitates were formed subsequently, as shown in Fig. 8. This is also consistent with the results of SEM in Fig. 3f.

In summary, the typical hierarchical structures in as-SLMed H13 steel contained the relatively coarse matrix grains (0.5–11 μm), fine cellular structures (~0.6 μm) and nano-scale carbides (~20 nm), detected by SEM and EBSD as well as

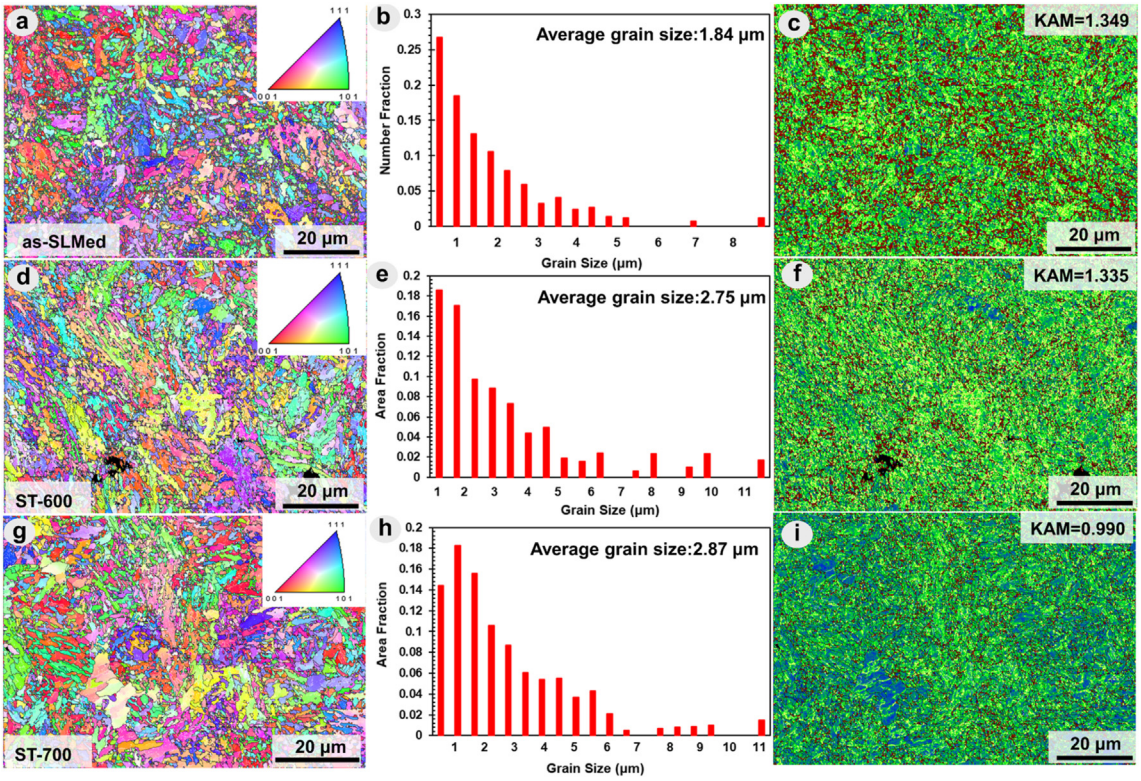

Fig. 5 – EBSD maps, grain size distribution maps and kernel average misorientation (KAM) maps: (a–c) as-SLMed sample; (d–f) ST-600 sample; (g–i) ST-700 sample.

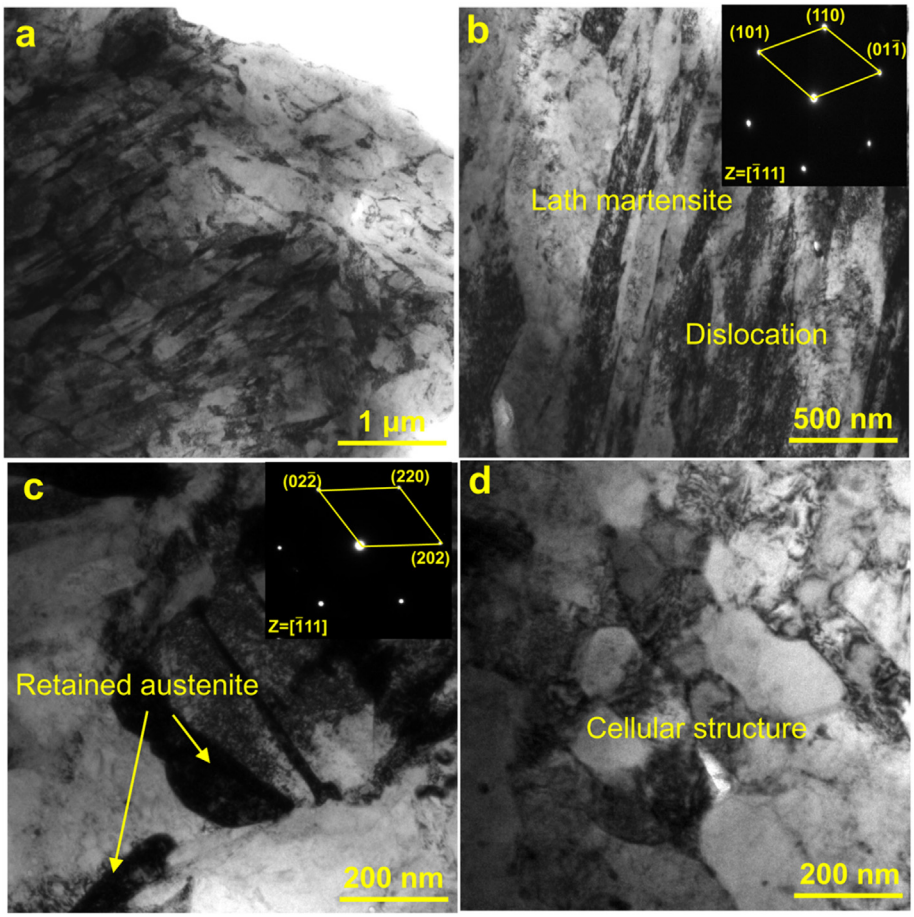

Fig. 6 – (a–d) BF-TEM micrographs of as-SLMed alloy showing (a, b) lath martensite with dislocations and corresponding SAED pattern; (c) retained austenite and corresponding SAED pattern; (d) cellular structures.

TEM. A typical schematic diagram to show the dissolution of cellular structures and the formation of carbide precipitates in H13 alloy is illustrated in Fig. 9 under as-SLMed and as-tempered conditions. Under as-SLMed condition, the microstructure consists of lath martensite and cellular structures (Fig. 9a). The relatively coarse grains contain fine cellular structure and lath martensite as well as high-volume fraction of retained austenite, as shown in the schematic image of Fig. 9a, combined with the results of SEM/EBSD/TEM. Under as-tempered condition, after tempering at 600 °C for 1 h, the size of matrix grains increase from 1.84 to 2.75 μm; The morphology of partially dissolved cellular structure was determined by Fig. 3b and 7d; Also, fine $M_{23}C_6$ precipitates was detected in the microstructure. These characteristics are all reflected in the schematic image of Fig. 9b. When the tempering is carried out at higher temperature of 700 °C (Fig. 9c), the cellular structures are completely dissolved and a large amount of coarse $M_{23}C_6$ carbide precipitates are formed. These can be attributed to the increase of driving force for element diffusion at increased temperature [39]. The coalescence of carbides results in the coarsening of carbides [40]. The volume fraction of retained austenite is significantly decreased to 4%.

3.2. *Mechanical properties*

The tensile stress-strain curves of as-SLMed, ST-600 and ST-700 samples are shown in Fig. 10. It is seen that the YS, UTS, and El of the as-SLMed H13 steel were 1468 ± 23 MPa, 1837 ± 27 MPa, and 8.5 ± 0.6%, respectively. The YS and UTS of the ST-600 sample increased to 1647 ± 29 MPa and 2013 ± 35 MPa, respectively, but the El reduced to 4.1 ± 0.3%. Clearly, the strength of ST-600 sample was superior to those under as-SLMed condition. For the ST-700 sample, the YS, UTS and El were 887 ± 18 MPa, 1083 ± 21 MPa and 12.3 ± 1.2%. The YS and UTS decreased significantly in comparison with that of the as-SLMed and ST-600 samples. Fig. 10b shows a comparison of tensile strength of H13 steel manufactured by different techniques, including conventional casting methods [18,41,42], SLM [[1,2,23,28,43]] and SLM + heat treatment [28,34,41]in both other literatures and this study. Obviously, the ST-600 and ST-700 samples showed a good balance between strength and ductility.

Fig. 11 shows the SEM micrographs of fractured surface. It is seen that the fractured surface of as-SLMed sample contained microvoids and the cleavage fracture pattern, as shown in Fig. 11a. Microvoids may act as sites for dimples based on

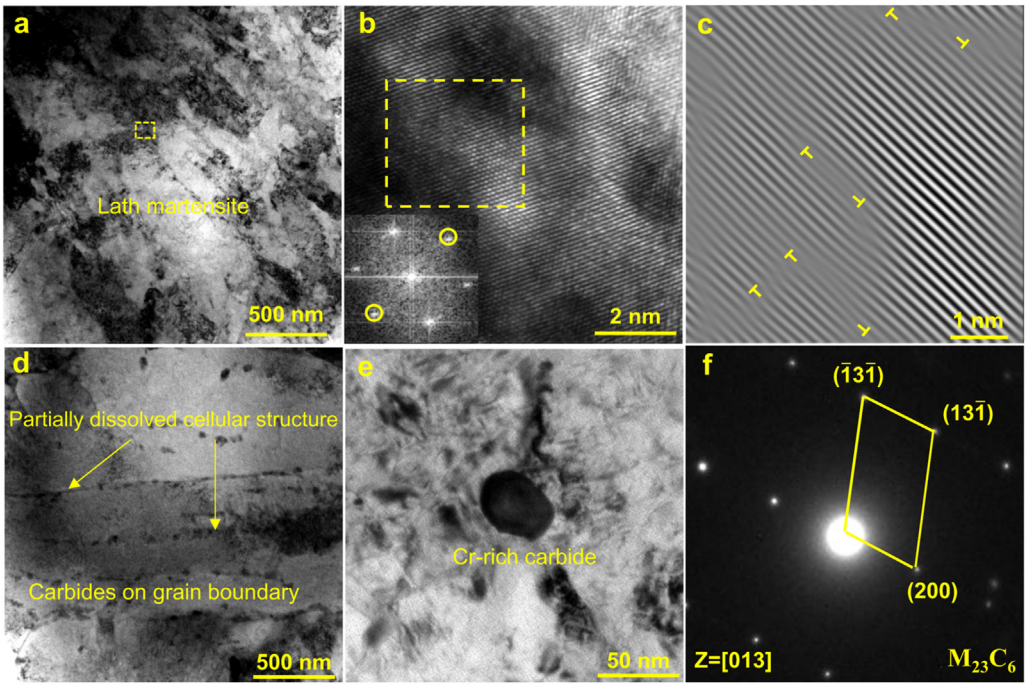

Fig. 7 – (a–f) BF-TEM and HR-TEM micrographs of ST-600 sample showing (a) lath martensite with dislocations; (b) HR-TEM image of the marked area in (a) with inserted FFT pattern; (c) Fourier-filtered image of the marked area in (b), showing high-density dislocations (marked by "T"); (d) carbides at grain boundary of cellular structures; (e) and (f) $M_{23}C_6$ carbide and corresponding SAED pattern.

the mechanism of microvoid coalescence [44]. Correspondingly, a certain number of dimples were observed in Fig. 11b, indicating that the fracture mode was ductile-brittle combination. For the ST-600 sample, the shallower depth of dimples was formed, confirming the weak elongation (Fig. 11d). However, the number density of dimples was obviously increased in the ST-700 sample, confirming the increase of ductility (Fig. 11e&f).

In summary, the mechanical properties of H13 steel are determined by microstructural characteristics, including the matrix grain structures, precipitates and dislocation density, which are influenced by tempering treatment. For the as-SLMed H13 alloy, potential strengthening mechanisms include the combination of grain boundary strengthening (σ_g), dislocation strengthening (σ_{dis}), cellular structure strengthening (σ_c) and precipitation strengthening (σ_p), in addition to its lattice friction strength σ_0. For simplicity, the contribution of main mechanisms responsible for strengthening of H13 alloy can be expressed as:

$$\sigma_y = \sigma_0 + \sigma_g + \sigma_{dis} + \sigma_c + \sigma_p \quad (3)$$

where σ_0 is a constant (70 MPa for H13 alloy [45]).

3.2.1 *Grain boundary strengthening*

The grain boundary strengthening (σ_g) can be estimated via the Hall-Petch relationship as follow:

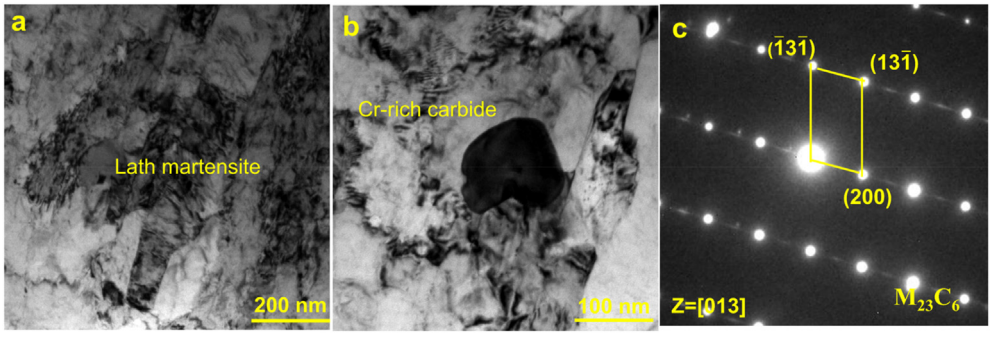

Fig. 8 – (a–c) TEM micrographs of ST-700 sample; (a) the BF-TEM image showing the formation of lath martensite; (b, c) BF-TEM images and SAED patterns showing the formation of coarse $M_{23}C_6$ carbides.

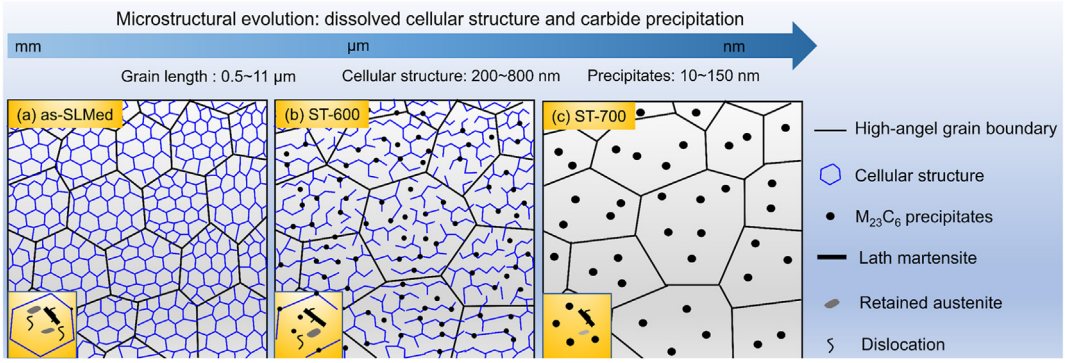

Fig. 9 – Schematic diagram showing microstructural evolution of SLMed H13 steel under the condition of (a) as-SLMed; (b) ST-600; (c) ST-700.

$$\sigma_g = K \times d^{-1/2} \tag{4}$$

where K is the Hall-Petch constant, and d is the average grain size. The K (572 MPa $\mu m^{1/2}$) is taken from literatures [46,47].

3.2.2Dislocation strengthening

The dislocation strengthening (σ_{dis}) can be evaluated via a variant of Taylor equation [48]:

$$\sigma_{dis} = C \times \sqrt{\rho} \tag{5}$$

where C is 7.34 × 10^{-6} MPa/m and ρ is the dislocation density. The dislocation density is calculated based on the KAM value.

3.2.3Cellular structure strengthening

The cellular structure strengthening (σ_c) can be evaluated via following equation [29]:

$$\sigma_c = 183.31 + 253.66 \Big/ \sqrt{Lc} \tag{6}$$

The average diameter of cellular structures has been applied to scale one of the strength criteria for as-SLMed steels [29]. Based on SEM results, we used Image Pro Plus software to count corresponding *Lc* (582.8 nm).

3.2.4Precipitation strengthening

The precipitation strengthening can be calculated through the Orowan by pass mechanism [49,50]:

$$\sigma_p = \frac{0.538Gbf_i^{1/2}}{r_i} \times ln\left(\frac{r_i}{2b}\right) \tag{7}$$

where G is the shear modulus (80 GPa) [51], b is the burger vector (0.25 nm) [51], f_i is the volume fraction of precipitates, and r_i is the mean size of precipitates.

Based on TEM results, the volume fraction and the mean size of carbides is 1.8% and 21.2 nm, respectively, which is calculated by Image Pro Plus software. In addition, the σ_p shows an inverse relationship with the particle size, and vice versa for the volume fraction. The strengthening contribution was neglected because of no carbides in the as-SLMed sample and the insignificant coarse carbides (>100 nm) in ST-700 sample.

The multiple strengthening mechanisms can be calculated using Eq. (3). Fig. 12 shows a comparison of contributions to yield strength from calculation and from experimental measurement. According to the calculation, the yield strength of the as-SLMed alloy is 1546.2 MPa, which is very close to the data obtained from experimental measurement. The cellular

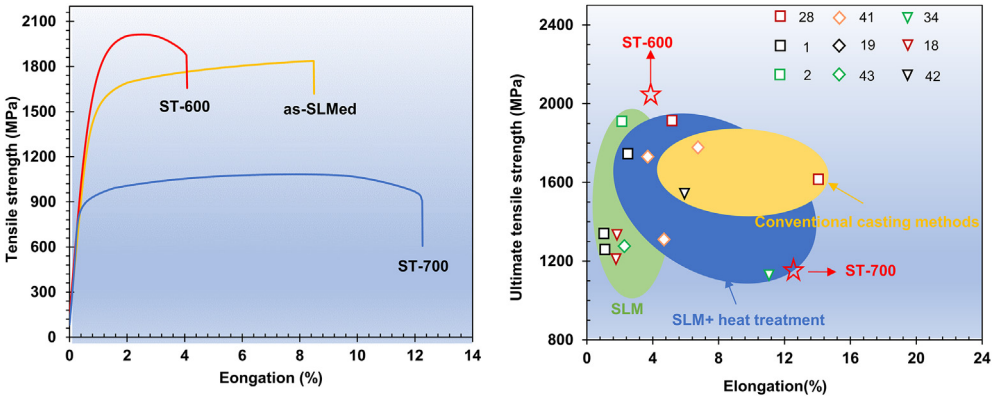

Fig. 10 – (a) Tensile stress-strain curves of as-SLMed, ST600 and ST-700 samples; (b) Comparison of tensile strength of H13 steel manufactured by different techniques, including conventional casting methods [18,41,42], SLM [[1,2,23,28,43]], SLM + heat treatment [28,34,41].

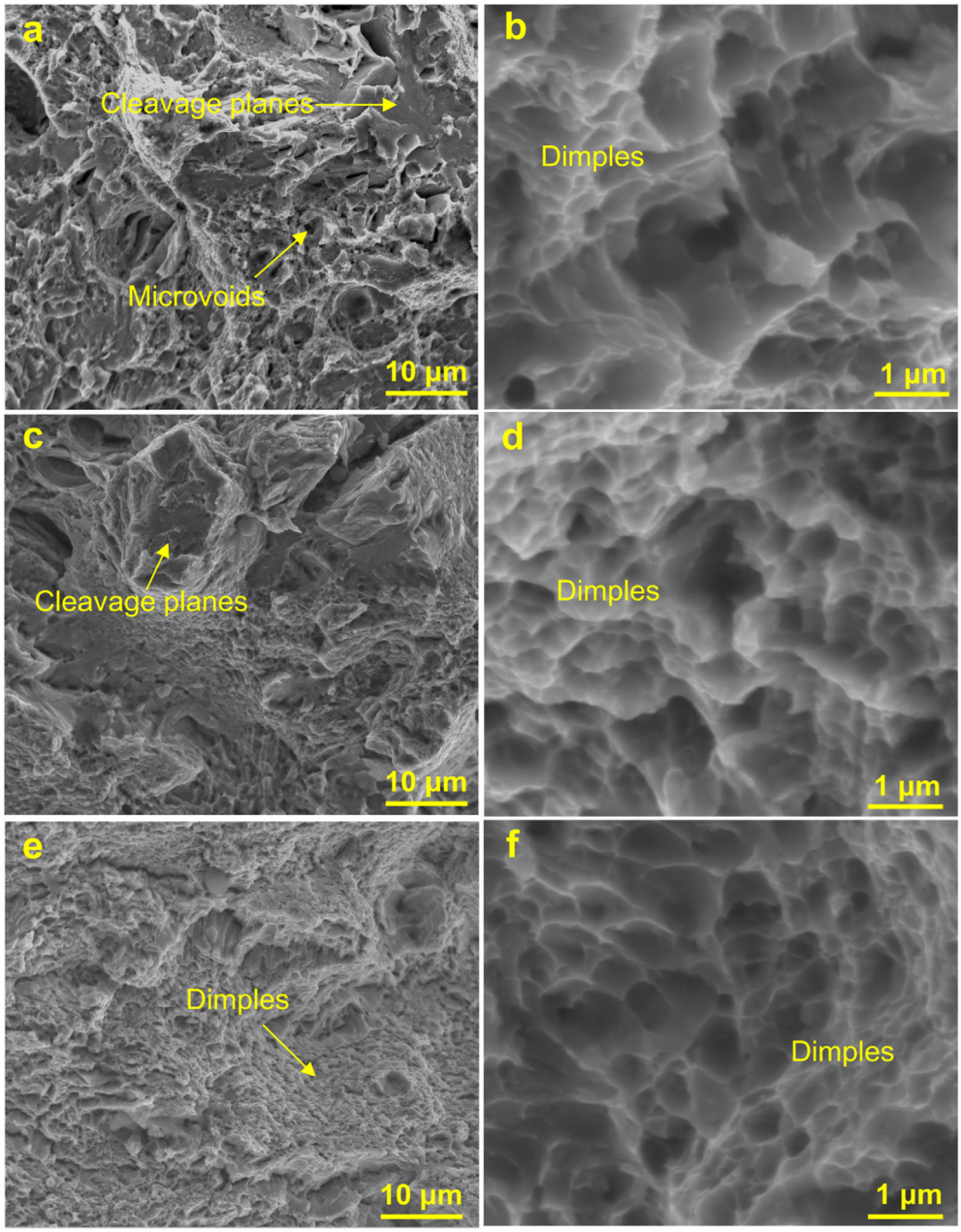

Fig. 11 – SEM micrographs of fractured surfaces and high magnifications; (a–b) as-SLMed sample; (c–d) ST-600 sample; (e–f) ST-700 sample.

structure, the fine grain size and the dislocation induced by the thermal contraction stress during the rapid solidification of SLM process are the main contributors of the high strength.

Tempering heat treatment can effectively eliminate residual stresses and retained austenite formed during SLM process. Generally, tempering leads to recovery of dislocations, relaxation of highly deformed supersaturated martensite and the dissolved cellular structures. These can cause a reduction of strength. However, tempering at 300–600 °C of as-SLMed H13 steel generates secondary hardening by introducing the high number density of nanoscale carbides. In ST-600 sample, the characteristics of cellular structures are still preserved while nanoscales $M_{23}C_6$-type carbides are formed and pinned at the sub-boundaries in cellular structures. Furthermore, there is no significant change in the dislocation density in comparison with that in the as-SLMed sample. Therefore, the strength contribution is mainly from precipitation strengthening, grain boundary strengthening and dislocation strengthening and cellular structure strengthening. Since the partial dissolution of cellular structures is not modelled in the theoretical equations, the calculated yield strength in the ST-600 sample is higher than the experimental data. With increased tempering temperature at 700 °C, the cellular structures are completely dissolved. Meanwhile, the carbides further grow up to a level of over 100 nm. The effect of precipitation strengthening is

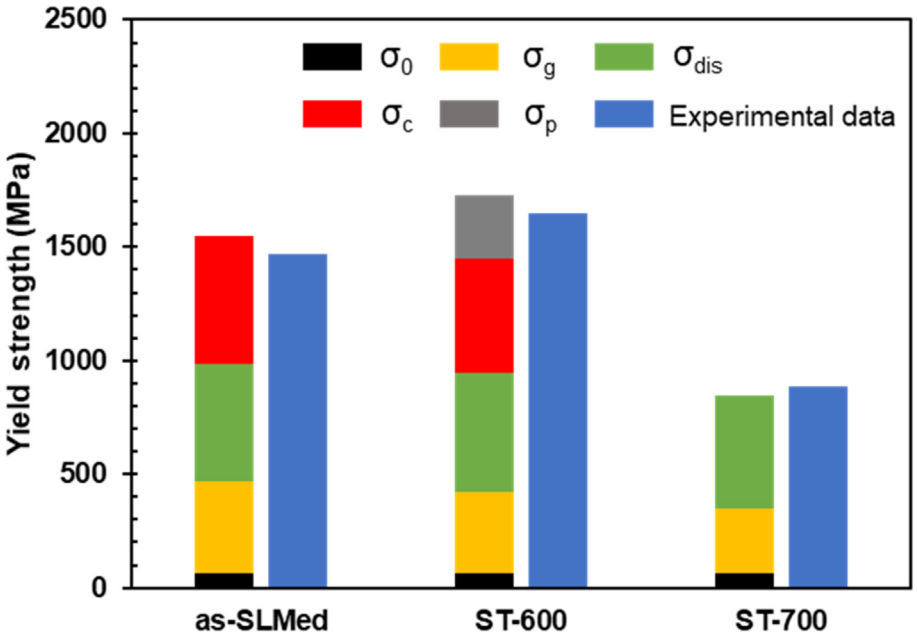

Fig. 12 – Comparison of yield strength from calculated results and the experimental measurement.

diminished and negligible. Therefore, the yield strength of the ST-700 sample is mainly contributed by grain boundary and precipitation strengthening.

4. Conclusions

In this work, H13 steel processed by SLM and the effects of tempering treatment on the microstructural evolution and mechanical properties was studied. The major conclusions findings can be drawn as follows:

(1) The as-SLMed H13 steel consisted of cellular structures, lath martensite and high-volume of retained austenite. After tempering at 600 °C for 1 h, the matrix transformed from the supersaturated martensite to the tempered lath martensite, followed by a partial recovery of dislocations. And, the cellular structures are partially dissolved, while nanoscale $M_{23}C_6$ carbides were formed at the boundaries. After tempering at 700 °C for 1 h, the cellular structures were completely dissolved, the retained austenite content was further reduced, while high number density of coarse $M_{23}C_6$ carbides were formed as precipitation.

(2) In the as-SLMed H13 steel, the yield strength, UTS and elongation was 1468 ± 23 MPa, 1837 ± 27 MPa and 8.5 ± 0.6%, respectively. In the sample tempered at 600 °C for 1 h, the yield strength increased to 1647 ± 29 MPa, the UTS increased to 2013 ± 35 MPa, but the elongation decreased to 4.1 ± 0 0.3%. The outstanding yield strength was attributed to the fine $Cr_{23}C_6$precipitates pinned the boundaries of cellular structures in chains, fine grains and high number density of dislocations. In the samples tempered at 700 °C for 1 h, the elongation significantly increased to 12.3 ± 1.2% while both yield strength and UTS decreased. The recovery of dislocation density and relaxation and the decomposition of martensite were responsible for the significant improvement in elongation.

(3) Selecting the appropriate tempering to overcome the trade-off between the decrease of strength induced by dissolved cellular structures and the improvement in strength induced by carbide precipitation was an effective strategy way to achieve high strength or high ductility of SLMed H13 steel.

Declaration of Competing Interest

The authors declare that they have no known competing financial interests or personal relationships that could have appeared to influence the work reported in this paper.

Acknowledgement

Financial support from the National Key Research and Development Program of China (Grant No. 2020YFB0311300ZL), National Natural Science Foundation of China (Grant No. 52071343).

REFERENCES

[1] Åsberg M, Fredriksson G, Hatami S, Fredriksson W, Krakhmalev P. Influence of post treatment on microstructure, porosity and mechanical properties of additive manufactured H13 tool steel. Mater Sci Eng, A 2019;742:584–9.

[2] Mazur M, Brincat P, Leary M, Brandt M. Numerical and experimental evaluation of a conformally cooled H13 steel

injection mould manufactured with selective laser melting. Int J Adv Manuf Technol 2017;93:881–900.
[3] Srinivas M, Babu BS. A critical review on recent research methodologies in additive manufacturing. Mater Today Proc 2017;4(8):9049–59.
[4] Zeng GH, Song T, Dai YH, Tang HP, Yan M. 3D printed breathable mould steel: small micrometer-sized, interconnected pores by creatively introducing foaming agent to additive manufacturing. Mater Des 2019;169(5):107693.
[5] Li HX, Qi HL, Song CH, Li YL, Yan M. Selective laser melting of P20 mould steel: investigation on the resultant microstructure, high-temperature hardness and corrosion resistance. Powder Metall 2017;61(1):21–7.
[6] Fette M, Sander P, Wulfsberg J, Zierk H, Herrmann A, Stoess N. Optimized and cost-efficient compression molds manufactured by selective laser melting for the production of thermoset fiber reinforced plastic aircraft components. Procedia CIRP 2015;35:25–33.
[7] Herzog D, Seyda V, Wycisk E, Emmelmann C. Additive manufacturing of metals. Acta Mater 2016;117:371–92.
[8] Debroy T, Wei HL, Zuback J, Mukherjee T, Zhang W. Additive manufacturing of metallic components – process, structure and properties. Prog Mater Sci 2018;92:112–224.
[9] Wang JT, Liu SP, Fang YP, He ZR. A short review on selective laser melting of H13 steel. Int J Adv Manuf Technol 2020;108:2453–66.
[10] Deirrmina F, Peghini N, Almangour B, Frzesiak D, Pellizzari M. Heat treatment and properties of a hot work tool steel fabricated by additive manufacturing. Mater Sci Eng, A 2019;753(10):109–21.
[11] Mertens R, Vrancken B, Holmstock N, Kinds Y, Kruth JP, Humbeeck JV. Influence of powder bed preheating on microstructure and mechanical properties of H13 tool steel SLM parts. Phys Procedia 2016;83:882–90.
[12] Yan JJ, Zheng DL, Li HX, Jia X, Sun JF, Li YL, et al. Selective laser melting of H13: microstructure and residual stress. J Mater Sci 2017;52:12476–85.
[13] Ren B, Lu D, Zhou R, Li Z, Guan J. Preparation and mechanical properties of selective laser melted H13 steel. J Mater Res 2019;34:1415–25.
[14] Bajaj P, Hariharan A, Kini A, Kürnsteiner P, Raabe D, Jägle EA. Steels in additive manufacturing: a review of their microstructure and properties. Mater Sci Eng, A 2020;772(20):138633.
[15] Narvan M, Al-Rubaie KS, Elbestawi M. Process-structure-Property relationships of AISI H13 tool steel processed with selective laser melting. Materials 2019;12(14):2284.
[16] Lei F, Wen T, Yang FP, Wang JY, Fu JW, Yang HL, et al. Microstructures and mechanical properties of H13 tool steel processed by selective laser melting. Materials 2022;15:2686.
[17] Krell J, R€ottger A, Geenen K, Theisen W. General investigations on processing tool steel X40CrMoV5-1 with selective laser melting. J Mater Process Technol 2018;255:679–88.
[18] Wang M, Wu Y, Wei Q, Shi Y. Thermal fatigue properties of H13 Hot-work tool steels processed by selective laser melting. Metals 2020;10(1):1–17.
[19] Maziasz PJ, Payzant EA, Schlienger ME, Mchugh KM. Residual stresses and microstructure of H13 steel formed by combining two different direct fabrication methods. Scripta Mater 1998;39(10):1471–6.
[20] Cottam R, Wang J, Luzin V. Characterization of microstructure and residual stress in a 3D H13 tool steel component produced by additive manufacturing. J Mater Res 2014;29(17):1978–86.
[21] Xue L, Chen J, Wang SH. Freeform laser consolidated H13 and CPM 9V tool steels. Microsc Microanal 2013;2(2):67–78.
[22] Ning AG, Mao WW, Chen XC, Guo HJ, Guo J. Precipitation behavior of carbides in H13 hot work die steel and its strengthening during tempering. Metals 2017;7(3):1–15.
[23] Lima EPR, Maurício DM, Neves D. Effect of different tempering stages and temperatures on microstructure, tenacity and hardness of vacuum sintered HSS AISI T15. Mater Sci Forum 2008;591–593:68–73.
[24] Holzweissig MJ, Brenne ATF, Schaper M, Niendorf T. Microstructural characterization and mechanical performance of hot work tool steel processed by selective laser melting. Metall Mater Trans B 2015;46:545–9.
[25] Wang M, Li W, Wu Y, Li S, Cai C, Wen SF, et al. High-temperature properties and microstructural stability of the AISI H13 hot-work tool steel processed by selective laser melting. Metall Mater Trans B 2019;50:531–42.
[26] Chen CJ, Yan K, Qin L, Zhang M, Wang X, Zou T, et al. Effect of heat treatment on microstructure and mechanical properties of laser additively manufactured AISI H13 tool steel. J Mater Eng Perform 2017;26(11):5577–89.
[27] Katancik M, Mirzababaei S, Ghayoor M, Pasebani S. Selective laser melting and tempering of H13 tool steel for rapid tooling applications. J Alloys Compd 2020;849(30):156319.
[28] Yan JJ, Song H, Dong YP, Quach WM, Yan M. High strength (~2000 MPa) or highly ductile (~11%) additively manufacturedH13 by tempering at different conditions. Mater Sci Eng, A 2020;773:138845.
[29] Wang YM, Voisin T, McKeown JT, Ye JC, Calta NP, Li Z, et al. Additively manufactured hierarchical stainless steels with high strength and ductility. Nat Mater 2018;17(1):63–70.
[30] Zhong Y, Liu LF, Wikman S, Cui DQ, Shen ZJ. Intragranular cellular segregation network structure strengthening 316L stainless steel prepared by selective laser melting. J Nucl Mater 2016;470:170–8.
[31] Guo SM, Jiang Z, Wu JJ, Qie XY, Yu T, Guo KY, et al. Research on a tunable monochromatic X-rays source in (5~40) keV. Appl Radiat Isot 2022;181:110096.
[32] Bi J, Lei ZL, Chen YB, Chen X, Lu NN, Tian Z, et al. An additively manufactured Al-14.1Mg-0.47Si-0.31Sc-0.17Zr alloy with high specific strength, good thermal stability and excellent corrosion resistance. J Mater Sci Technol 2021;67:23–35.
[33] Syed AK, Ahmad B, Guo H, Machry T, Eatock D, Meyer J, et al. An experimental study of residual stress and direction-dependence of fatigue crack growth behavior in as-built and stress-relieved selective-laser melted Ti6Al4V. Mater Sci Eng, A 2019;755:246–57.
[34] Yuan MW, Cao Y, Karamchedu S, Hosseini S, Yao YM, Berglund J, et al. Characteristics of a modified H13 hot-work tool steel fabricated by means of laser beam powder bed fusion. Mater Sci Eng, A 2022;831(13):142322.
[35] Yang HL, Zhang YY, Wang JY, Liu ZL, Liu CH, Ji SX. Additive manufacturing of a high strength Al-5Mg2Si-2Mg alloy: microstructure and mechanical properties. J Mater Sci Technol 2021;91:215–23.
[36] Ai XH, Wang JY, Wen T, Yang FP, Dong XX, Yang HL, et al. A high Fe-containing AlSi12 alloy fabricated by laser powder bed fusion. J Mater Res Technol 2020;18:4513–21.
[37] Wang JY, Zou JP, Yang HL, Zhang LJ, Liu ZL, Dong XX, et al. Exceptional strength-ductility synergy of additively manufactured CoCrNi medium-entropy alloy achieved by lattice defects in heterogeneous microstructures. J Mater Sci Technol 2022;127(10):61–70.
[38] Wang JY, Zou JP, Yang HL, Liu ZL, Ji SX. High strength and ductility of an additively manufactured CrCoNi medium-entropy alloy achieved by minor Mo doping. Mater Sci Eng, A 2022;843(23):143129.
[39] Pan Y, Pi ZQ, Liu BW, Xu W, Zhang C, Qu XH, et al. Influence of heat treatment on the microstructural evolution and

mechanical properties of W6Mo5Cr4V2Co5Nb (825 K) high speed steel. Mater Sci Eng, A 2020;787:139480.
[40] Gu JB, Li JY, Yanagimoto J, Li W, Li LH. Microstructural evolution and mechanical property changes of a new nitrogen-alloyed Cr-Mo-V hot-working die steel during tempering. Mater Sci Eng, A 2021;804(4):140721.
[41] Lee J, Choe J, Park J, Yu JH, Kim S, Jung ID, et al. Microstructural effects on the tensile and fracture behavior of selective laser melted H13 tool steel under varying conditions. Mater Charact 2019;155:109817.
[42] Li FY, Ma DS, Chen ZZ, Liu JH, Youg QL, Kang Z. Structure and properties of high temperature diffused-superfining treated die Steel H13. Spec Steel 2008;9:63–5.
[43] Safka J, Ackermann M, Voleský L. Structural properties of H13 tool steel parts produced with use of selective laser melting technology. J Phys Conf Ser 2016;709:012004.
[44] Bhuiyan MS, Toda H, Uesugi K, Takeuchi A, Watanabe. Damage micromechanisms in high Mn and Zn content 7XXX aluminum alloys. Mater Sci Eng, A 2020;793:139423.
[45] Li Q. Modeling the microstructure–mechanical property relationship for a 12Cr–2W–V–Mo–Ni power plant steel. Mater Sci Eng, A 2003;25:385–91.
[46] Mao WW, Ning AG, Guo HJ. Nanoscale precipitates and comprehensive strengthening mechanism in AISI H13 steel. Int J Min Metall Mater 2016;23:1056–64.
[47] Majta J, Lenard JG, Pietrzyk M. A study of the effect of the thermomechanical history on the mechanical properties of a high niobium steel. Mater Sci Eng, A 1996;208:249–59.
[48] Sun XW, Wang YF, Sun DY, Jia Xin, Zhao T, Zhang FC, et al. Microstructure and mechanical properties of Si-rich H13 steel processed via austempering and tempering. Mater Sci Eng, A 2022;834:142616.
[49] Liang JW, Shen YF, Misra RDK, Liaw PK. High strength-superplasticity combination of ultrafine-grained ferritic steel: the significant role of nanoscale carbides. J Mater Sci Technol 2021;83:131–44.
[50] Jia N, Shen YF, Liang JW, Feng XW, Wang HB, Misra RDK. Nanoscale spheroidized cementite induced ultrahigh strength-ductility combination in innovatively processed ultrafine-grained low alloy medium-carbon steel. Sci Rep 2017;7(1):2679.
[51] Mazaheri Y, Kermanpur A, Najafizadeh A. Strengthening mechanisms of ultrafine grained dual phase steels developed by new thermomechanical processing. ISIJ Int 2015;55:218–26.